

Photoactivatable Lipids

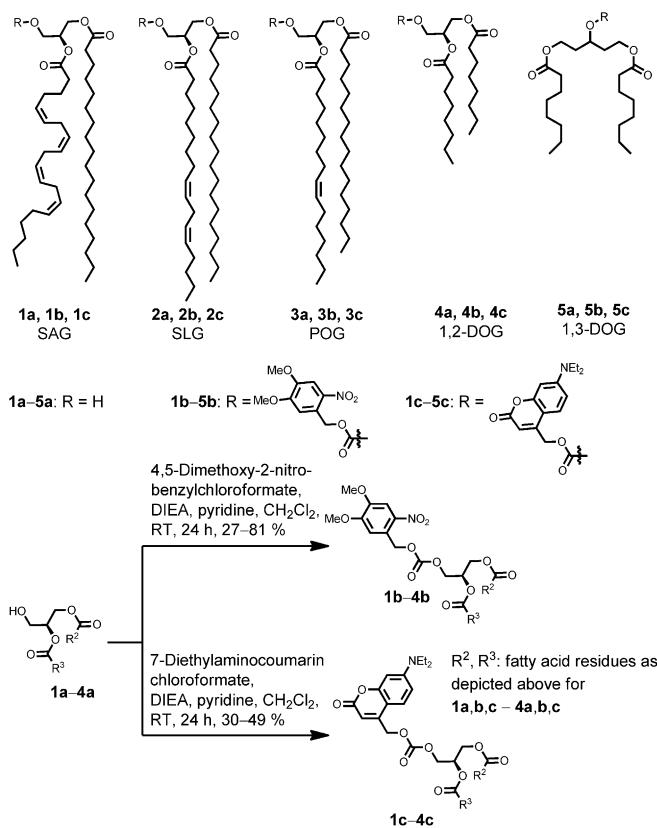
# The Fatty Acid Composition of Diacylglycerols Determines Local Signaling Patterns\*\*

André Nadler, Gregor Reither, Suihan Feng, Frank Stein, Sabine Reither, Rainer Müller, and Carsten Schultz\*

Cellular signals are transduced through vast networks of proteins and small molecule metabolites. Rigorous control of the respective signaling molecules is required to ensure a precise and reproducible outcome. On the protein level this is often accomplished by specific reversible chemical modifications such as phosphorylation or by localization of proteins to defined cellular compartments.<sup>[1,2]</sup> Much less is known about cellular mechanisms that control small-molecule-mediated signaling events. This is largely due to the intrinsically more difficult observation of small-molecule turnover and localization in living cells. These difficulties are potentiated when lipid signaling is investigated. The variety of known lipid backbones is fairly comprehensive but the diversity and combinations of fatty acids attached to these backbones provides many thousand possibilities and lipidomics shows that a large portion of this diversity is available in cells.<sup>[3–5]</sup> This overwhelming and generally not addressable complexity has led to a situation where lipid signaling events are treated as head-group signaling events and the existing chemical differences between individual species of the same lipid class are widely ignored although a number of *in vitro* studies suggest significant differences in potency.<sup>[6–8]</sup> Along the same lines, the influence of subcellular concentration gradients of defined lipid species on intracellular signaling has not been studied thoroughly so far. We hypothesized that both lipid species diversity and subcellular concentration gradients of distinct lipid species might serve as molecular mechanisms to drive specific lipid-mediated signaling events.

Experimentally, both fatty acid diversity and locally elevated levels of a given species may be generated by using photoactivatable lipids in intact cells.<sup>[9–11]</sup> We chose to analyze diacylglycerol (DAG) signaling due to its important role in several cellular signaling pathways that include G-protein coupled receptors as well as growth factor triggered and

calcium-based signaling networks.<sup>[12–15]</sup> Recent lipidomics analyses demonstrated the co-existence of 30–50 DAG species with different fatty acid compositions in mammalian cells.<sup>[3–5]</sup> While DAGs are best known to activate various protein kinase C (PKC) isoforms by binding to their C1 domains and recruiting them to cellular membranes,<sup>[16,17]</sup> DAG-induced translocation and activation of proteins such as RasGRPs, Munc13, and DGK $\gamma$  have also been described.<sup>[18,19]</sup> In addition, DAGs have been shown to directly activate human transient receptor potential C3 (TRPC3) and TRPC6 channels.<sup>[20–22]</sup> So far, locally elevated DAG levels have either been experimentally achieved by liberation of a photoactivatable T-cell receptor agonist which causes downstream DAG production or by local uncaging of a non-physiological DAG analogue.<sup>[9,23]</sup> While these approaches have led to important insights into the mechanism of T-cell receptor mediated signaling and microtubule-organizing center (MTOC) polarization in T-cells, they cannot be utilized



**Scheme 1.** Structures of diacylglycerols **1a–5a** and synthesis of the respective coumarinylmethylene- and nitroveratroyl-caged derivatives.

[\*] Dr. A. Nadler,<sup>[†]</sup> Dr. G. Reither,<sup>[†]</sup> S. Feng, F. Stein, Dr. S. Reither, Dr. R. Müller, Priv.-Doz. Dr. C. Schultz  
Cell Biology & Biophysics Unit  
European Molecular Biology Laboratory  
Meyerhofstrasse 1, 69117 Heidelberg (Germany)  
E-mail: schultz@embl.de

[†] These authors contributed equally to this work.

[\*\*] We thank the Advanced Light Microscopy Facility (ALMF) of EMBL for expert support in microscopy. We acknowledge financial support by the DFG (Transregio 83).

Supporting information for this article (including synthetic procedures, analytical data, additional information concerning conducted experiments, and a brief characterization of the utilized biosensors) is available on the WWW under <http://dx.doi.org/10.1002/anie.201301716>.

to investigate the potential differences in the biological activity of distinct DAG species. Here we introduce a set of photoactivatable (caged) DAGs that feature different fatty acid compositions in order to address this question.

The design of caged DAGs is straightforward as the obvious attachment point of the cage is the single hydroxy group (Scheme 1). In order to attach two different fatty acids, we employed a recently developed synthetic route that permits the stepwise introduction of different fatty acids and features a final deprotection procedure that fully avoids fatty acid migration, a common problem in DAG syntheses.<sup>[24]</sup> We employed two different caging groups, a fluorescent coumarinylmethylene variety as well as the more standard, nonfluorescent 4,5-dimethoxy-2-nitrobenzyl (nitroveratroyl) group, both attached through a carbonate linker.

The two variants were used in a complementary way, as their intrinsic properties make them especially suited for different experiments. The coumarinylmethylene group is cleaved by 405 nm light and enables two-photon uncaging. Furthermore, its intrinsic fluorescence can be used to quantify compound loading into cells when the biological activity of different compounds needs to be assessed. On the other hand, the relatively broad emission spectrum of coumarin effectively limits the available spectral range for multiparameter live-cell imaging to the spectral region above 500 nm. In the case of the nonfluorescent 4,5-dimethoxy-2-nitrobenzyl (nitroveratroyl) group, the entire spectrum remains available, but photoactivation has to be performed at 366–375 nm, which might be phototoxic to cells. We prepared a set of five different DAGs, three of them from DAGs with natural fatty acid compositions (SAG = stearyl-arachidonyl glycerol (**1a**), SLG = stearyl-linolenyl (**2a**), POG = palmitoyl-oleyl (**3a**), as well as the commonly used nonnatural 1,2-di-*O*-octanoyl glycerol (1,2-DOG, **4a**) and its inactive 1,3-isomer **5a** which serves as negative control throughout this study (Scheme 1, see the Supporting Information for details). The photoactivatable groups were attached through chloroformates in acceptable to good yields and gave the respective DAGs as nitroveratroyl (**1b–5b**) and coumarinylmethylene (**1c–5c**) carbonate esters.

We chose HeLa cells as a model system for live cell application of the caged DAGs and used a double scanner confocal microscope (Olympus FV1000) in order to combine uncaging through the microscope objective with simultaneous live cell imaging. We quantified the compound uptake of the coumarin-caged DAGs by measuring coumarin fluorescence and devised a protocol that warranted comparable compound loading for intracellular photoactivation experiments (see Supporting Information for details). All caged compounds were essentially inactive when applied to cells expressing suitable biosensors. Successful photoreactions were confirmed by experiments using a C1-GFP translocation probe<sup>[25]</sup> and the caged 1,2-DOG (**4b**, **4c**) or the inactive 1,3-DOG (**5b**, **5c**) (Figure 1). Global plasma membrane translocation was observed in each extracellular 1,2-DOG photoactivation experiment for both nitroveratroyl- and coumarin-caged variants but not for 1,3-DOG photoactivation. Intracellular photoactivation gave comparable results (Figure S3 in the Supporting Information). Interestingly,

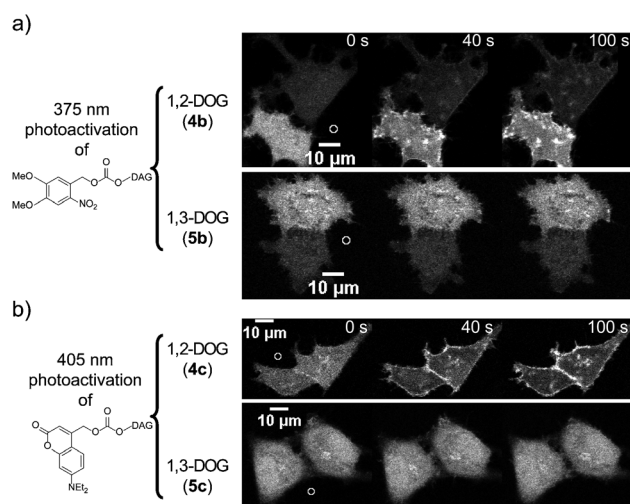


**Figure 1.** Compound release by local extracellular photoactivation of 1,2-DOG and 1,3-DOG monitored by translocation of the C1-GFP translocation probe. The imaging medium contained  $30 \mu\text{mol L}^{-1}$  of the respective compounds **4b**, **5b**, **4c**, and **5c**. a) Time-lapse montages of photoactivation experiments with 1,2-DOG (**4b**, **5b**, 375 nm) and 1,3-DOG (**4c**, **5c**, 405 nm). The indicated areas (white circles) were irradiated for 10 s starting at  $t = 15$  s. The quantification of the observed translocation events is described in the Supporting Information.

photoactivation of the naturally occurring SAG (**1b**) frequently resulted in spatially confined translocation events as opposed to 1,2-DOG (**4b**) (Figure S4 in the Supporting Information).

According to transcriptome analysis, the utilized HeLa cells expressed human TRPC3 and TRPC6 channels, allowing us to compare the potency of different DAG species. We initially used the nitroveratroyl-caged DAGs in combination with the genetically encoded ratiometric GEM-GECO sensor for  $\text{Ca}^{2+}$  imaging.<sup>[26]</sup> We found a massive increase in intracellular  $\text{Ca}^{2+}$  levels when SAG was photoactivated and an intermediate response for SLG, whereas neither POG nor 1,2-DOG displayed a significant potency for triggering  $\text{Ca}^{2+}$  transients (Figure 2a). Detailed analysis of individual traces obtained by photoactivation of SAG and SLG showed that SLG generally induced fewer, shorter, and less intense events. SAG induced long-lasting  $\text{Ca}^{2+}$  elevations which were similar in amplitude to that after ionomycin treatment, indicating that the  $\text{Ca}^{2+}$  concentration was at least locally in the micromolar range (Figure S5 in the Supporting Information). To make sure that the observed  $\text{Ca}^{2+}$  transients were indeed induced by SAG and not by its metabolites, we prepared caged arachidonic acid and compared the  $\text{Ca}^{2+}$  transients induced by photoactivation. We found that SAG was significantly more potent, thereby emphasizing its role as initial signaling molecule (Figure S6 in the Supporting Information). To confirm the observed structure–activity relationship, we used the coumarin-caged DAGs in combination with the genetically encoded green-emitting G-GECO  $\text{Ca}^{2+}$  sensor which does not interfere with coumarin emission.<sup>[26]</sup> Again, SAG was identified as the by far most potent species, followed by SLG, whereas the other three lipids were largely inactive

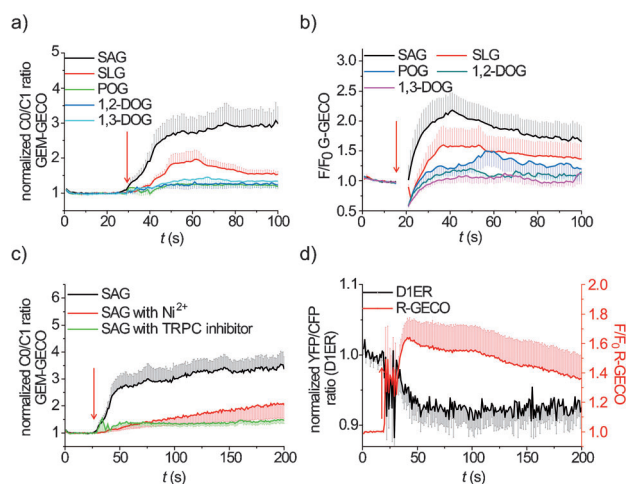


**Figure 2.** Local  $\text{Ca}^{2+}$  signals upon intracellular DAG photoactivation in HeLa cells were monitored using the genetically encoded GEM-GECO, R-GECO, G-GECO, or the ratiometric D1ER  $\text{Ca}^{2+}$  sensor. Ratio or intensity changes were measured in regions of interest of similar size spatially close to the site of irradiation. Normalized mean ratio or intensity changes are plotted as a function of time, the shaded area above or below each curve indicates half of the standard error of the mean at each given point. C0 = blue emission, C1 = green emission. a)  $\text{Ca}^{2+}$  transients upon photoactivation of nitroveratrolyl-caged DAG species (**1b–5b**, red arrow) or b) coumarin-caged DAG species (**1c–5c**). c) Inhibition of the SAG (**1b**)-induced calcium transients by addition of  $\text{NiCl}_2$  ( $1 \text{ mmol L}^{-1}$ ) or the TRP channel inhibitor SKF-96365 ( $50 \mu\text{mol L}^{-1}$ ) prior to 375 nm photoactivation. d) Simultaneous detection of  $\text{Ca}^{2+}$  levels in the cytosol and endoplasmic reticulum (ER) upon SAG (**1b**) photoactivation in cells transiently expressing R-GECO and D1ER.

(Figure 2b). The overall appearance of false-positive  $\text{Ca}^{2+}$  signals was slightly higher for coumarin-caged DAGs, indicating that the photoreaction by itself might not be completely innocent with respect to  $\text{Ca}^{2+}$  signaling.

To identify the  $\text{Ca}^{2+}$  source, we performed a series of SAG (**1b**, dimethoxynitrobenzyl cage) uncaging experiments in the presence of either  $1 \text{ mmol L}^{-1}$   $\text{NiCl}_2$  for the unspecific blocking of calcium channels or  $50 \mu\text{mol L}^{-1}$  SKF-96365, a selective inhibitor of human TRPC3 and TRPC6 channels.<sup>[27]</sup> DAG-induced increases of  $\text{Ca}^{2+}$  levels were almost completely suppressed in both cases. In addition, the calcium increase was barely altered after addition of the inositol triphosphate receptor blocker Xestospongine C (Figure S6 in the Supporting Information). This indicates that at least the initial event was due to  $\text{Ca}^{2+}$  influx through TRPC channels (Figure 2c). It is conceivable that in the subsequent response, calcium influx from the extracellular space and the endoplasmic reticulum (ER) is contributing.<sup>[29]</sup> This is supported by simultaneous measurement of ER (with D1ER)<sup>[28]</sup> and cytosolic  $\text{Ca}^{2+}$  levels (with R-GECO, a red-emitting, genetically encoded cytosolic  $\text{Ca}^{2+}$  sensor). ER levels showed a significant drop, while the cytosolic concentration increased (Figure 2d). The  $\text{Ca}^{2+}$  signals were vastly diminished in both compartments when the TRP channel blocker SKF-96365 was applied. This demonstrates that TRP channel opening is the initial event (Figure S6 in the Supporting Information).

In order to address the downstream effects of DAG photoactivation we chose to study PKC $\alpha$  recruitment to the plasma membrane simultaneously with changes in  $[\text{Ca}^{2+}]_i$  and used transiently expressed PKC $\alpha$ -EGFP and R-GECO in HeLa cells. Physiological translocation of PKC $\alpha$  requires both an increase in calcium and DAG levels.<sup>[30]</sup> We performed local DAG (**1b–5b**) photoactivation experiments and frequently observed local PKC $\alpha$  accumulation in the vicinity of the irradiation site after SAG uncaging, whereas none of the other DAGs induced comparable local events (Figure 3a,b). The observed calcium transients for individual DAGs showed a dependence on fatty acid composition similar to that observed before (Figure S7 in the Supporting Information). Careful data analysis made it possible to dissect the observed phenotype into a number of distinct events. SAG photoactivation initially caused a massive  $\text{Ca}^{2+}$  transient (19 out of 20 experiments), which in a few cases (4 out of 20) was followed by  $\text{Ca}^{2+}$ -driven global PKC $\alpha$  translocation. In contrast to these rather short-lived events, PKC $\alpha$  accumulation was most frequently observed in the immediate vicinity of the irradiation site (14 out of 20). Both translocation events exhibited distinctly different onset and decay kinetics. Furthermore, the local PKC events were generally accompanied by locally elevated  $\text{Ca}^{2+}$  levels. To address the question of which cellular membranes are the actual locations of the observed local PKC $\alpha$  translocation events, we performed SAG photoactivation experiments in cells transiently expressing PKC $\alpha$ -EGFP and GPI-mRFP to stain the plasma membrane or PKC $\alpha$ -EGFP and mCherry-KDEL to stain the ER. We found clear co-localization of the translocated PKC $\alpha$  fraction with the plasma membrane marker (Figure 3f) but not with the ER marker (Figure S8 in the Supporting Information), indicating that the major fraction of the membrane-bound PKC $\alpha$  was located at the plasma membrane.

To describe the observed events in a more quantitative way, we developed a macro for the ImageJ image analysis software, which made it possible to quantify the size of the regions of elevated  $\text{Ca}^{2+}$  levels and PKC $\alpha$  accumulation in an automated way and also determine the mean relative fluorescence intensity change ( $F/F_0$ ) in the regions of interest. A detailed description of the procedure and the source code of the macro can be found in the Supporting Information.

By using this approach, we were able to correlate the spread and intensity of the observed PKC $\alpha$  and  $\text{Ca}^{2+}$  signals. The  $\text{Ca}^{2+}$  signal reached much further than the significantly more localized PKC $\alpha$  accumulation (Figure 3c). The SAG-induced  $\text{Ca}^{2+}$  signal displayed rapid onset kinetics in spatial reach and intensity, culminating approximately 40 s after the irradiation period at an average reach of  $45 \pm 8\%$  of the total cell size and an average  $F/F_0$  value of  $2.0 \pm 0.1$ . The spread of the  $\text{Ca}^{2+}$  signal subsequently decreased monotonically until an average value of  $15 \pm 3\%$  of the total cell size was reached after 250 s. The average intensity in the respective detected areas exhibited strikingly different kinetics. After an initial transient the average  $F/F_0$  values increased significantly (Figure S9 in the Supporting Information). This indicates that two qualitatively different  $\text{Ca}^{2+}$  signals took place at the same time—a global, relatively transient event and a much

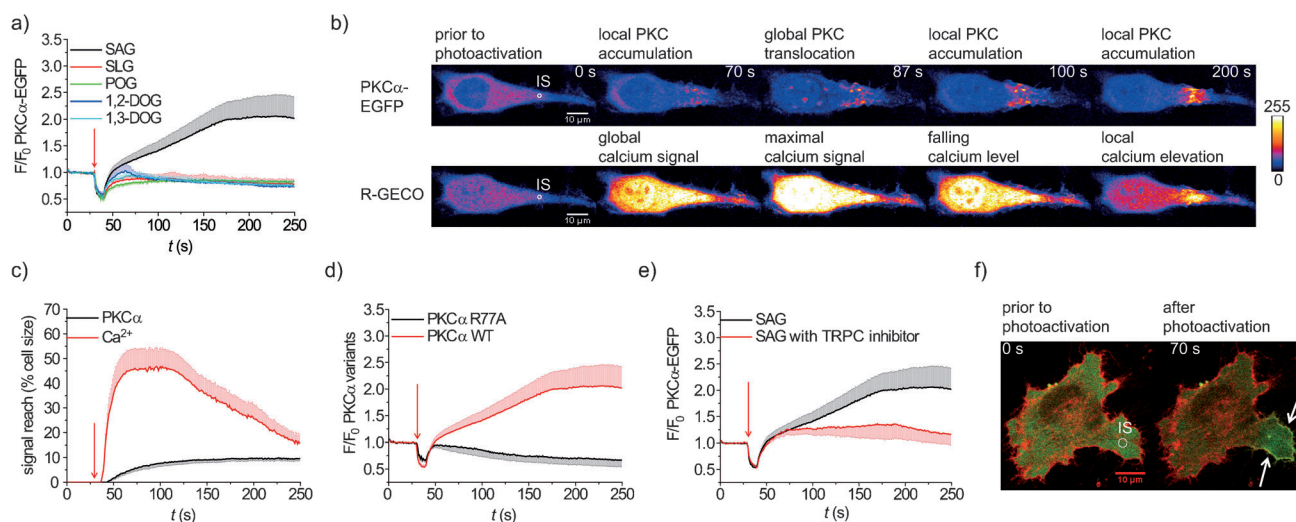


**Figure 3.** DAG (1b–5b) photoactivation in PKC $\alpha$ -EGFP/R-GECO double-transfected HeLa cells ( $t=30$  s for 10 s at the illumination site (IS)). Red arrows indicate the start of photoactivation in time traces. a) Comparison of induced local PKC $\alpha$  accumulation upon photoactivation of nitroveratroyl-caged DAGs. Intensity changes were measured in regions of interest of similar size spatially close to the uncaging site. Normalized mean intensity changes are plotted as a function of time, the shaded area above or below each curve indicates half of the standard error of the mean at each given point. b) Time-lapse montages of PKC $\alpha$ -EGFP and R-GECO responses after SAG (1b) uncaging. c) Quantification of the reach of PKC $\alpha$  and Ca $^{2+}$  signals after SAG (1b) uncaging. d) Comparison of PKC accumulation in HeLa cell transfected with either PKC $\alpha$ -EGFP or PKC $\alpha$ R77A-EGFP after SAG (1b) uncaging. e) PKC $\alpha$  accumulation (expressed as  $F/F_0$ ) at the illumination site in cells expressing PKC $\alpha$ -EGFP in the presence or absence of the TRPC channel inhibitor SKF-96365 after SAG (1b) uncaging. f) Colocalization of PKC $\alpha$ -EGFP (green) and GPI-MRFP (red) after SAG (1b) uncaging. White arrows indicate local PKC $\alpha$  translocation to the plasma membrane.

longer lasting local one which occurred in the area of PKC $\alpha$  accumulation and is likely fully dependent on TRPC channel opening (Figure 3e). The observed average PKC accumulation exhibited much slower onset kinetics in both monitored parameters, with the local signal spread reaching a plateau at  $10 \pm 1\%$  of the total cell size after approximately 150 s and the average  $F/F_0$  value increasing over the complete observation period (Figure 3c, Figure S9 in the Supporting Information).

To address the importance of direct DAG–PKC $\alpha$  interaction, we performed SAG photoactivation in HeLa cells transiently expressing R-GECO and PKC $\alpha$ R77A-EGFP, a PKC $\alpha$  variant bearing a point mutation within the C1 domain which greatly diminishes the DAG binding capability. We found that this protein did not accumulate at the irradiation site (Figure 3d), indicating that direct PKC–DAG interaction is essential for the local pattern. The observed Ca $^{2+}$  signals occurred with the same frequency but were generally less intense and far reaching. Importantly, the average intensity course in the respective detected areas did not exhibit the characteristic double-maximum shape indicative of long-lasting local Ca $^{2+}$  elevations (Figure S8 in the Supporting Information). A possible explanation might be a positive feedback between PKC $\alpha$  and Ca $^{2+}$  signals, which is impaired in the absence of a direct DAG–PKC $\alpha$  interaction and local PKC activity.

It has been previously shown that a number of DAG-metabolizing enzymes maintain a certain specificity for individual DAG species depending on their fatty acid composition.<sup>[8,31,32]</sup> Following this finding, it has been suggested that these differences reflect the need for a much

tighter metabolic control of actual signaling species such as SAG.<sup>[33]</sup> Our data indicate for the first time that lipid composition, metabolism, and effectiveness of lipid recognition are very relevant for the output of a cellular PKC–Ca $^{2+}$ -signaling network. Especially in lipid signaling, the diffusion-reaction mechanisms might be a common reason for the formation of different signal patterns.

Our combined results demonstrate that cells can respond to a given spatially confined signal both with a local and a global response pattern. Local signaling is important in polarized and migrating cells, in particular, where signaling at one of the membranes has to produce locally different molecular events. Another example might be membrane repair after physical membrane injury, where a large local calcium influx induces a local repair mechanism. Full analysis and modeling of the signaling network should lead to further insight into the complex regulation of local signaling events. It remains to be shown if other lipids such as the phosphoinositides known to be crucial for cell polarity are locally regulated by similar mechanisms and whether the fatty acid composition is of similar importance. Future studies should address the large diversity in the fatty acid composition of lipids not only because of the difference in intrinsic signaling activity but also in lipid metabolism and the resulting lifetime of a given species. For these studies, caged lipids will be invaluable tools.

Received: February 27, 2013

**Keywords:** caged lipids · diacylglycerol · fatty acid composition · protein kinase C · signaling networks

- [1] J. Groves, J. Kuriyan, *Nat. Struct. Mol. Biol.* **2010**, *17*, 659–665.
- [2] R. P. Bhattacharyya, A. Reményi, B. J. Yeh, W. A. Lim, *Annu. Rev. Biochem.* **2006**, *75*, 655–680.
- [3] O. Quehenberger, A. M. Armando, A. H. Brown, S. B. Milne, D. S. Myers, A. H. Merrill, S. Bandyopadhyay, K. N. Jones, S. Kelly, R. L. Shaner, C. M. Sullards, E. Wang, R. C. Murphy, R. M. Barkley, T. J. Leiker, C. R. H. Raetz, Z. Guan, G. M. Laird, D. A. Six, D. W. Russell, J. G. McDonald, S. Subramaniam, E. Fahy, E. A. Dennis, *J. Lipid Res.* **2010**, *51*, 3299–3305.
- [4] J. L. Sampaio, M. J. Gerl, C. Klose, C. S. Ejsing, H. Beug, K. Simons, A. Shevchenko, *Proc. Natl. Acad. Sci. USA* **2011**, *108*, 1903–1907.
- [5] E. A. Dennis, R. A. Deems, R. Harkewicz, O. Quehenberger, H. A. Brown, S. B. Milne, D. S. Myers, C. K. Glass, G. Hardiman, D. Reichart, A. H. Merrill, Jr., M. C. Sullards, E. Wang, R. C. Murphy, C. R. Raetz, T. A. Garrett, Z. Guan, A. C. Ryan, D. W. Russell, J. G. McDonald, B. M. Thompson, W. A. Shaw, M. Sud, Y. Zhao, S. Gupta, M. R. Maurya, E. Fahy, S. Subramaniam, *J. Biol. Chem.* **2010**, *285*, 39976–39985.
- [6] S. Madani, A. Hichami, A. Legrand, J. Belleville, N. A. Khan, *FASEB J.* **2001**, *15*, 2595–2601.
- [7] M. N. Hodgkin, T. R. Pettitt, A. Martin, R. H. Michell, A. J. Pemberton, M. J. Wakelam, *Trends Biochem. Sci.* **1998**, *23*, 200–204.
- [8] W. Tang, M. Bunting, G. A. Zimmerman, T. M. McIntyre, S. M. Prescott, *J. Biol. Chem.* **1996**, *271*, 10237–10241.
- [9] E. J. Quann, E. Merino, T. Furuta, M. Huse, *Nat. Immunol.* **2009**, *10*, 627–635.
- [10] D. Subramanian, V. Laketa, R. Müller, C. Tischer, S. Zerbakhsh, R. Pepperkok, C. Schultz, *Nat. Chem. Biol.* **2010**, *6*, 324–326.
- [11] M. Mentel, V. Laketa, D. Subramanian, H. Gilland, C. Schultz, *Angew. Chem.* **2011**, *123*, 3895–3898; *Angew. Chem. Int. Ed.* **2011**, *50*, 3811–3814.
- [12] B. Ananthanarayanan, R. V. Stahelin, M. A. Digman, W. Cho, *J. Biol. Chem.* **2003**, *278*, 46886–46894.
- [13] S. Carrasco, I. Mérida, *Trends Biochem. Sci.* **2007**, *32*, 27–36.
- [14] Q. J. Wang, *Trends Pharmacol. Sci.* **2006**, *27*, 317–323.
- [15] K. Oda, Y. Matsuoka, A. Funahashi, H. Kitano, *Mol. Biosyst.* **2005**, *1*, 1–17.
- [16] J. Giorgione, M. Hysell, D. F. Harvey, A. C. Newton, *Biochemistry* **2003**, *42*, 11194–11202.
- [17] A. C. Newton, *Am. J. Physiol. Endocrinol. Metabol.* **2010**, *298*, E395–E402.
- [18] C. Yang, M. G. Kazanietz, *Trends Pharmacol. Sci.* **2003**, *24*, 602–608.
- [19] N. Brose, *J. Cell Sci.* **2002**, *115*, 4399–4411.
- [20] T. Hofmann, A. G. Obukhov, M. Schaefer, C. Harteneck, T. Gudermann, G. Schultz, *Nature* **1999**, *397*, 259–263.
- [21] G. Vazquez, J.-Y. Tano, K. Smedlund, *Channels* **2010**, *4*, 232–240.
- [22] a) L. Lemonnier, M. Trebak, J. W. Putney, *Cell Calcium* **2008**, *43*, 506–514; b) B. Fuchs, M. Rupp, H. A. Ghofrani, R. T. Schermuly, W. Seeger, F. Grimminger, T. Gudermann, A. Dietrich, N. Weissmann, *Respir. Res.* **2011**, *12*, 20–29.
- [23] a) M. Huse, L. O. Klein, A. T. Girvin, J. M. Faraj, Q.-J. Li, M. S. Kuhns, M. M. Davis, *Immunity* **2007**, *27*, 76–88; b) X. P. Huang, R. Sreekumar, J. R. Patel, J. W. Walker, *Biophys. J.* **1996**, *70*, 2448–2457; c) A. Z. Suzuki, T. Watanabe, M. Kawamoto, K. Nishiyama, H. Yamashita, M. Ishii, M. Iwamura, T. Furuta, *Org. Lett.* **2003**, *5*, 4867–4870.
- [24] R. J. Anderson, S. L. Osborne, F. A. Meunier, G. F. Painter, *J. Org. Chem.* **2010**, *75*, 3541–3551.
- [25] E. Oancea, M. N. Teruel, A. F. Quest, T. Meyer, *J. Cell Biol.* **1998**, *140*, 485–498.
- [26] Y. Zhao, S. Araki, J. Wu, T. Teramoto, Y.-F. Chang, M. Nakano, A. S. Abdelfattah, M. Fujiwara, T. Ishihara, T. Nagai, et al., *Science* **2011**, *333*, 1888–1891.
- [27] C. Harteneck, M. Gollasch, *Curr. Pharm. Biotechnol.* **2011**, *12*, 35–41.
- [28] A. E. Palmer, R. Y. Tsien, *Nat. Protoc.* **2006**, *1*, 1057–1065.
- [29] J. W. Putney, *Cell Calcium* **1986**, *7*, 1–12.
- [30] G. Reither, M. Schaefer, P. Lipp, *J. Cell Biol.* **2006**, *174*, 521–533.
- [31] K. D'Souza, R. M. Eppard, *J. Mol. Biol.* **2012**, *416*, 619–628.
- [32] T. O. Eichmann, M. Kumari, J. T. Haas, R. V. Farese, R. Zimmermann, A. Lass, R. Zechner, *J. Biol. Chem.* **2012**, *287*, 41446–41457.
- [33] M. J. Wakelam, *Biochim. Biophys. Acta Mol. Cell Biol. Lipids* **1998**, *1436*, 117–126.